communications physics

Article

https://doi.org/10.1038/s42005-024-01590-0

How turbulence spreading improves power handling in quiescent high confinement fusion plasmas

Zeyu Li[1] ✉, Xi Chen[1], Patrick. H. Diamond[2], Xueqiao Xu[3], Xijie Qin[4], Huiqian Wang[1], Filippo Scotti[3], Rongjie Hong[5], Guanying Yu[6], Zheng Yan[4], Filipp Khabanov[4] & George R. McKee[4]

Viable magnetic fusion devices necessitate combining good confinement with effective power flux handling. A major concern for ITER, and devices beyond, is the divertor heat load width, which sets peak boundary heat loads on the plasma-facing materials. Current estimates of the heat flux width are narrow for future reactors. Here, we demonstrate how pedestal turbulence can expand into, or entrain, the stable scrape-off-layer and so broaden the heat flux width beyond these neoclassical predictions. Employing combined theoretical, computational, and experimental approaches, we focus on quiescent high confinement discharges on the DIII-D tokamak, but the results are of broader significance. Our findings uncover common trends in the edge turbulence intensity flux, the pressure perturbation skewness, and the turbulence mixing length, which together determine the heat flux width. This research demonstrates the physics of scrape-off-layer broadening by turbulence and highlights the promise of a turbulent pedestal for successful core-edge integration in ITER and future fusion devices.

As worldwide consumption of energy and resources steadily increases, it is becoming more and more probable that traditional, non-renewable energy resources such as coal, oil, and natural gas will be depleted, and that the resulting carbonaceous products could have a significant impact on the global warming and environment. Fusion is a possible pathway to provide carbon-free, clean energy sources[1]. International Thermonuclear Experimental Reactor (ITER), an international collaboration project, is under construction for the purpose of validating the scientific and technological feasibility of fusion. One of the great challenges for ITER and future fusion reactors is handling the divertor target heat load while maintaining high core confinement. The divertor is a vessel component that extracts heat and ash produced by the fusion reaction. The design limit for the maximum ITER divertor heat load is 10 MW/m^2[2], which requires a sizeable heat load width to handle the fusion power flux on the divertor plasma-facing materials. Multi-machine divertor heat flux width scalings[3] imply a very narrow heat flux width λ_q (< 1 mm) for the ITER Q = 10 baseline scenario. To explain the present-day narrow heat flux widths in high-confinement mode (H-mode) plasmas, the *heuristic drift (HD)* model[4] was developed. The HD model ignores the turbulence in scrape-off-layer (SOL), as this is predicted to be quenched by the $E \times B$ shear. The HD model estimate combines cross-field magnetic drift velocity v_d with the parallel streaming dwell time $\tau_\parallel \sim 2qR/C_s$ to obtain $\lambda_q \sim v_d \tau_\parallel \sim 2\epsilon\rho_{\theta i}$. The result implies a narrow heat flux width (~ 2 mm) for ITER, where q, R, C_s, ϵ and $\rho_{\theta i}$ are the safety factor, major radius, ion sound speed, aspect ratio and poloidal ion gyro radius. Such a narrow λ_q could cause severe damage to the plasma-facing materials and threaten the safety of the ITER operation. Thus, there is considerable interest in broadening λ_q for ITER and future fusion devices.

Wider divertor heat flux widths for ITER are predicted by state-of-art numerical modeling using the XGC1[5] and BOUT++[6,7] simulation codes, due to edge turbulence which was ignored in the HD model. These studies claim that the edge turbulence could contribute to a stronger cross-field transport, and lead to a similar heat flux width near the marginally stable pedestal state, λ_q = 5.9 mm for XGC1 and λ_q ~ 5 mm for BOUT++. However, the underlying physical mechanisms for SOL turbulence production and its implications for SOL broadening remained unexplored, making it essential to address these questions for ITER. In this paper, we identify turbulence spreading as the key player and illuminate the physics of edge-to-SOL spreading. Theoretical models have studied the effect of turbulence spreading on the divertor heat flux width[8]. These predicted that both drift wave and ballooning mode turbulence in the pedestal could lead to

[1]General Atomics, San Diego, CA, USA. [2]University of California, San Diego, San Diego, CA, USA. [3]Lawrence Livermore National Laboratory, Livermore, CA, USA. [4]University of Wisconsin-Madison, Madison, WI, USA. [5]University of California, Los Angles, Los Angles, CA, USA. [6]University of California, Davis, Davis, CA, USA. ✉e-mail: lizeyu@fusion.gat.com

an enhanced turbulence intensity flux across the separatrix, thus broadening the SOL and heat flux widths. Experimental evidence relating turbulence spreading and the divertor heat flux width has also been observed in the large helical device (LHD)[9]. These works provide further insights into the physics that determines the divertor heat flux width. We also note that the transient pedestal events, such as edge localized modes (ELMs), could be triggered by the pedestal peeling-ballooning (PB) mode, and deposit large heat and particle flux to the divertor target, and so damage the plasma-facing components. Thus, developing a scenario with good confinement without ELMs, while maintaining a sizeable divertor heat flux width is a critical goal for the safe operation of future fusion reactors, like ITER and beyond.

This paper presents one possible realization of this goal in the Quiescent H-mode(QH mode). QH mode[10,11] and wide-pedestal QH mode[12,13] show the compatibility of high core confinement[14] and a quiescent edge, without ELMs. In recent QH mode experiments on the DIII-D tokamak, divertor heat flux width is observed to broaden following the increase of the pedestal broadband turbulence without driving edge harmonic oscillations (EHO)[15]. Separate experiments presented in this paper study the roles of the pedestal modes and the physics of turbulence spreading in setting the divertor heat flux width of DIII-D QH mode plasmas. The pedestal turbulence consists of a low-frequency ion diamagnetic direction (IDD) mode, which is radially extended from the pedestal top to the SOL; and a high-frequency electron diamagnetic direction (EDD) mode, which is radially peaked at the upper pedestal and localized in the pedestal location. In order to connect the upstream pedestal turbulence and downstream heat load width, this paper studies the roles of the pedestal modes and the physics of turbulence spreading in setting the divertor heat flux width of DIII-D QH mode plasmas. Here, we demonstrate how pedestal turbulence can expand into, or entrain, the stable scrape-off layer and so broaden the heat flux width beyond predicted neoclassical values. We show that the turbulence spreading is the mechanism, indeed the 'missing link', which connects pedestal turbulence to the heat load distribution on the downstream divertor.

Results

Experimental observations

The essential ingredients in the core-edge-boundary plasmas consist of the core region, SOL region, and divertor region. The separatrix sets the boundary between core and SOL plasmas. A schematic illustration of a QH mode cross-section on the DIII-D tokamak is shown in Fig. 1a. Broadband turbulence is widely observed in the pedestal region of wide-pedestal QH mode[16,17] and broadband QH mode[18] on DIII-D, which could have an impact on the heat flux width broadening as suggested by previous work[15]. Figure 1b, c shows the upstream midplane pedestal turbulence in a typical QH-mode and downstream divertor heat load pattern. Their relationship will be investigated in the following paper.

The broadband turbulences in the edge of QH mode have complex characteristics[16–19] as illustrated in Fig. 2, which contains the density fluctuation measured by the Beam Emission Spectroscopy (BES)[20] in one of the QH mode discharge #184902. In the upper pedestal region, i.e. $\psi_N = 0.90$ (blue) and 0.93 (green), broadband turbulence has dual bands (Fig. 2a, b). One band is a low-frequency (10–60 kHz) mode rotating in the ion diamagnetic direction (IDD) and the other band is in the high-frequency (60–200 kHz) range rotating in the electron diamagnetic direction (EDD), in the lab frame. At the pedestal peak gradient $\psi_N = 0.95$ (red), it is a combination of IDD and EDD mode in the mid-frequency mode (60–80 kHz) range, whose k_θ is kept almost constant regardless of the frequency. In the lower part of the pedestal $\psi_N = 0.98$ (purple) and SOL, the turbulence is dominated by the IDD mode for the whole frequency range (10–200 kHz). The radial mode structures resulting from the integration of different frequency ranges of IDD and EDD modes are depicted in Fig. 2c. The IDD mode, characterized by density perturbation $\delta n/n$, exhibits a larger mode amplitude, with its peak situated at the separatrix ($\psi_N = 1.0$), and a broader structure that extends farther into the SOL. Conversely, the EDD mode peaks at the upper pedestal, $\psi_N = 0.93$, and its influence barely reaches the SOL. The fundamental mechanism linking the pedestal turbulence and divertor heat flux width will be further analyzed numerically and theoretically in the latter part of this paper.

The divertor heat flux width of broadband QH mode for different plasma poloidal magnetic field B_p was measured in the recent QH mode experiments. The divertor strike point sweep technique was applied to obtain radially-resolved divertor heat load data from Divertor Langmuir Probes and Infrared Imaging Systems (IR camera). In Fig. 3a, heat flux widths are measured, and the comparison with the current multi-machine database is shown in Fig. 3a. The divertor heat flux width of broadband QH-mode also decreases with increasing poloidal magnetic

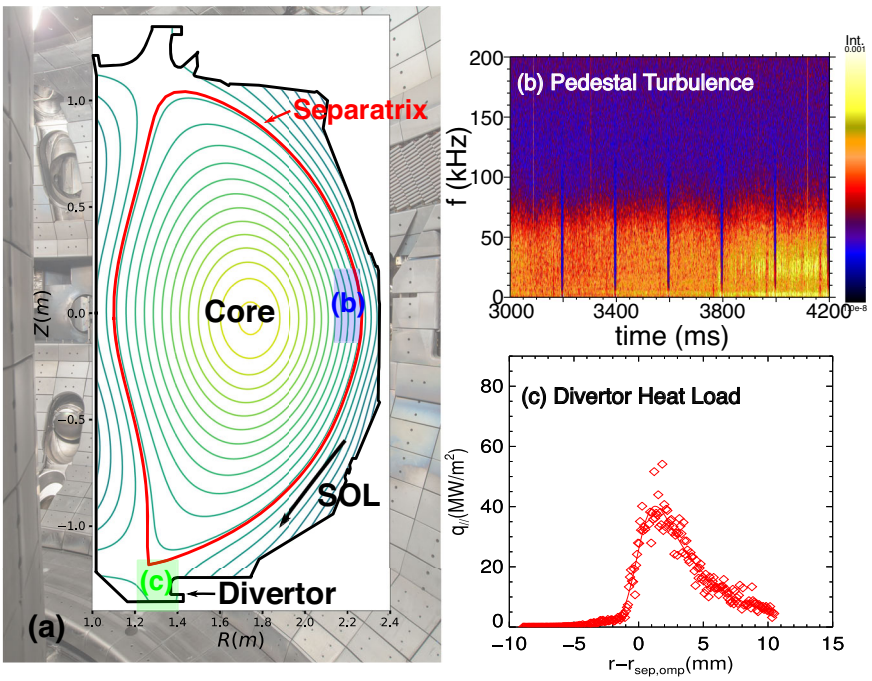

Fig. 1 | Schematic of DIII-D turbulent quiescent-H(QH) mode. a Illustration of DIII-D plasma cross-section; **b** Frequency spectrum of density turbulence perturbation as a function of time measured by Beam Emission Spectroscopy (BES) on the outboard-mid-plane, blue shaded **b** region in **a**. The color code gives the intensity of the turbulence; **c** Downstream divertor heat load pattern measured by Divertor Langmuir Probes, which shows the parallel heat load as a function of the distance to the separatrix mapped back to the outboard-mid-plane, green shaded **c** region in **a**.

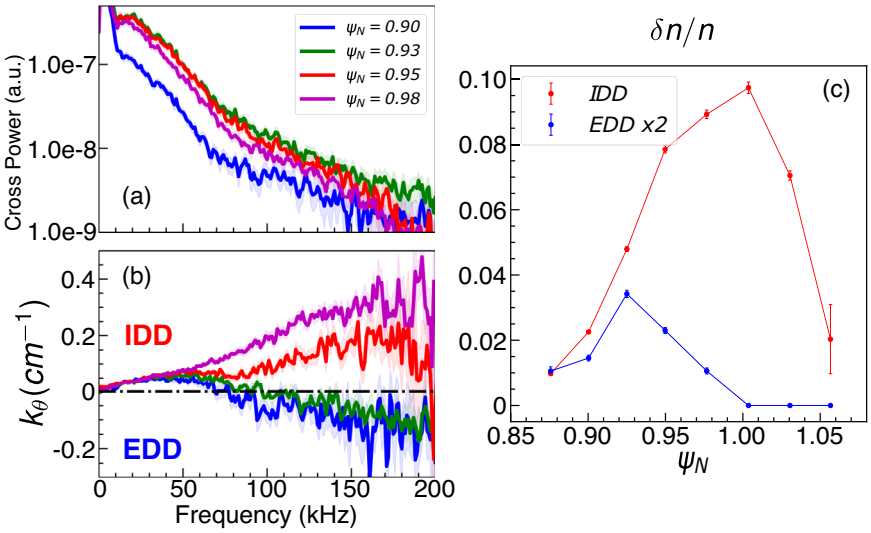

Fig. 2 | Broadband turbulence measured by Beam Emission Spectroscopy (BES) in the pedestal region of quiescent-H (QH) mode discharge #184902. a Cross power and **b** poloidal wave number k_θ as a function of frequency at different pedestal radial locations. The positive wave number shows the mode rotates in the ion diamagnetic direction (IDD) in the lab frame and the negative wave number shows the mode rotates in the electron diamagnetic direction (EDD) in the lab frame. **c** the radial envelope of density fluctuation ($\delta n/n$) associated with the IDD (red) and EDD (blue) mode. The error bar for the density fluctuation $\delta n/n$ is derived from the reciprocal of the square root of the coherence in the related frequency range.

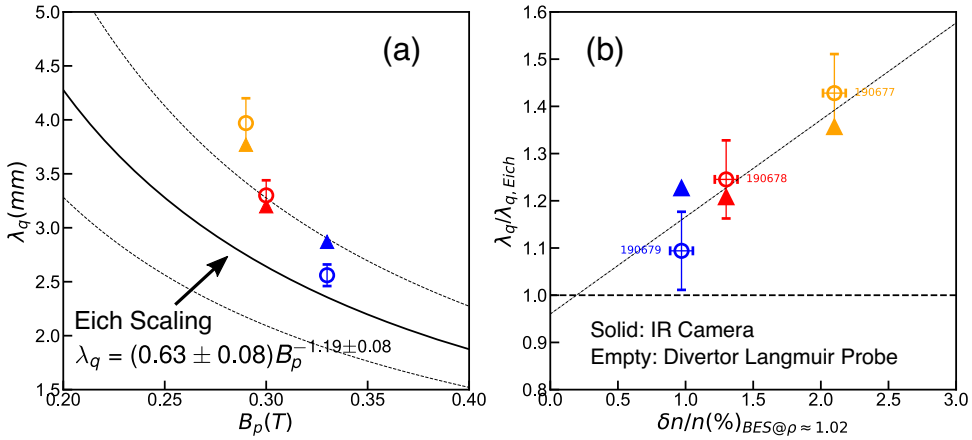

Fig. 3 | Divertor heat flux width with different out-mid-plane poloidal magnetic field Bp and turbulence at the separatrix. a Comparison of measured divertor heat flux width with experimental multi-machine scaling regression #14[52] (black); **b** Ratio of measured divertor heat flux and Eich scaling as a function of BES measured low-frequency IDD turbulence amplitude $\delta n/n$ close to the separatrix. Note that both ion diamagnetic direction (IDD) and electron diamagnetic direction (EDD) modes coexist inside the separatrix, and only IDD mode exists in the open field line region. The solid bullets are the heat flux width measured from Infrared Imaging Systems (IR camera), and the empty bullets are measured from Divertor Langmuir Probes. The errorbars are estimated by performing bootstrapping simulations for the heat flux widths measured by Divertor Langmuir Probes.

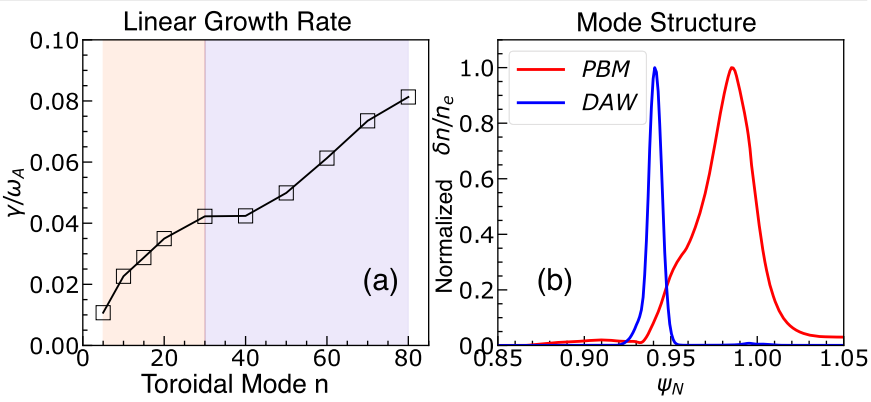

Fig. 4 | Linear modeling results for the DIII-D quiescent-H (QH) mode discharge #184902. a Linear growth rate γ/ω_A as a function of toroidal mode number n, where ω_A is the Alfvén frequency. The red-shaded region is the peeling-ballooning mode (PBM) dominant, and the blue-shaded region is drift Alfvén wave (DAW) dominant. The critical n_{crit} = 30 differentiates the PBM and DAW; **b** Radial mode structure of PBM and DAW.

field B_p along the hyperbola. The trend is due to the lowered safety factor q and thus shortened parallel dwell time $\tau_\parallel \sim 2qR/C_s$. The ratio of measured heat flux width to Eich scaling $\lambda_q/\lambda_{q,Eich}$ increases with the edge turbulence amplitude, shown in Fig. 3b. The horizontal axis shows the low-frequency (5–18 kHz) IDD turbulence measured by BES at the separatrix. Compared with the higher current discharges, the divertor heat flux widths still follow the trend of hyperbolic decrease with increasing B_p, but are broadened by stronger edge turbulence for the low-

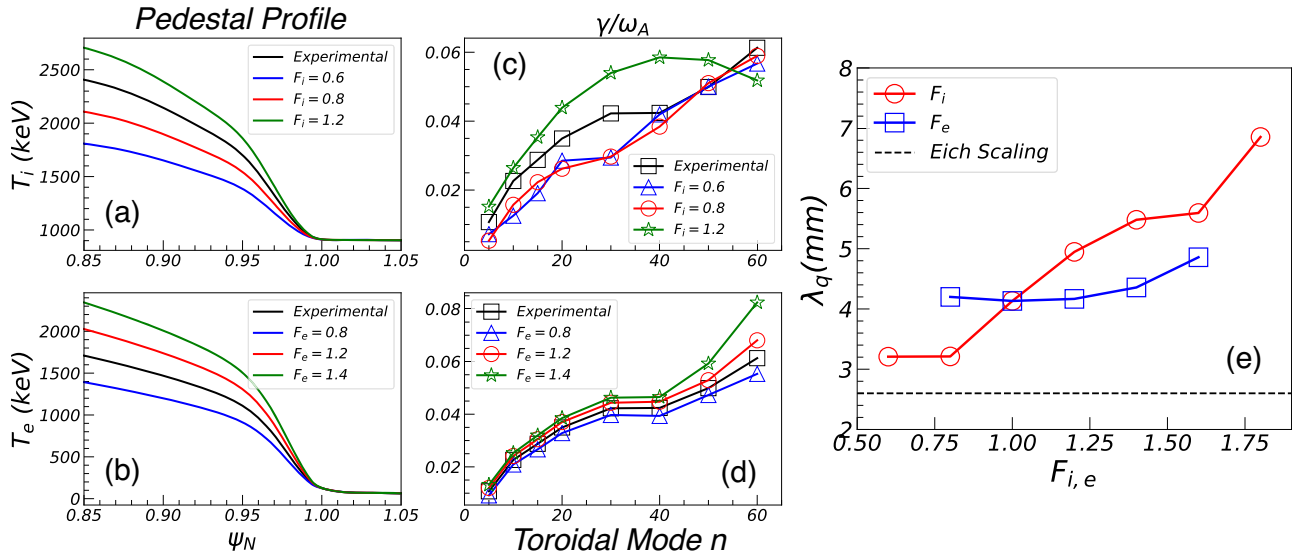

Fig. 5 | The changes in divertor heat flux widths correspond to the variations in pedestal conditions. Variation of pedestal ion temperature T_i **a** and electron temperature T_e **b** to change the linear growth rate of most unstable mode **c**, **d**. The critical transition n_{crit} increases with F_i while remains as, $n_{crit} = 30$, with F_e increases; **e** Divertor heat flux width λ_q as a function of pedestal scale factor F_i and F_e.

Table 1 | Characteristics of different modes of DIII-D QH mode in BOUT++ modeling

Mode	f, k_θ	Direction (lab frame)	Radial mode envelope	Driving mechanism	Stability	Impact on λ_q
Peeling-ballooning mode (PBM)	Low frequency, long wavelength	Ion diamagnetic	Pedestal top to SOL	Edge bootstrap current J_{BS} and pressure gradient ∇P	Sensitive to ∇T_i	Strong
Drift Alfvén Wave (DAW)	High frequency, intermediate-short wavelength	Electron diamagnetic	Localized at upper pedestal	Parallel passing electrons $\nabla n_e, \nabla T_e$	Sensitive to ∇T_e, insensitive to ∇T_i	Weak

B_p discharges(yellow). Note that the magnitude of λ_q was derived from the multi-scale scaling by increasing it by 40%

Numerical modeling

The role of broadband turbulence in broadening the divertor heat flux width is numerically investigated using the BOUT++ [21,22] six-field two-fluid model, which is widely utilized to study the edge physics and divertor heat flux width λ_q for several different current and future machines, C-Mod[23], DIII-D[24], EAST[25], ITER[5,6] and CFETR[26]. BOUT++ modeling achieved a reasonable agreement with experimental measurements on current machines[23–25], which normally follow Eich's scaling law and Goldston's heuristic drift model. For future reactors, like ITER and CFETR, the reduced radial drift velocity ($\sim 1/R$) could make the cross-field transport fall in a turbulence-dominant regime[5,6], while the underlying mechanism of how the SOL turbulence is generated and impacts heat load width must be determined. The BOUT++ six-field model with carbon impurity is implemented for the recent DIII-D QH mode discharges, which intends to understand the long-intermediate wave length edge turbulence within the fluid framework. Similar to previous work[19] the peeling-ballooning mode (PBM) and drift Alfvén wave (DAW) dominate for different toroidal mode numbers n, for the QH-mode discharge. The linear growth rate and linear mode structure are shown in Fig. 4. Linearly, PBM dominates at low to intermediate n, n = 5-30, and extends radially from the pedestal to the SOL; DAW turbulence dominates at higher n, $n > n_{crit} = 30$ and is localized radially at the upper pedestal $\psi_N = 0.93$–0.95. These results are consistent with the characteristics of the experimentally observed IDD and EDD mode shown in Fig. 2. A more detailed and quantitative comparison of linear and nonlinear simulation to the turbulence spectrum can be found in ref. 19

Simulations suggest that the spatially extended PBM turbulence plays a key role in broadening the divertor heat flux width λ_q beyond the Eich scaling prediction. The role of PBM and DAW in setting the divertor heat flux width in QH plasmas are investigated in numerical experiments where the pedestal ion temperature T_i and electron temperature T_e profiles are scaled up and down to change the relative amplitude of PBM and DAW. As illustrated in Fig. 5a, c, the pedestal profile inside the separatrix is scaled by the factor $F_{i,e}$, which ranges from 0.6 to 1.8. The SOL profiles are kept fixed to exclude the SOL profile effects on divertor heat load and its width. So the SOL remains linearly stable for all these cases. The linear growth rate of PBM increases with the T_i scale factor F_i, as shown in Fig. 5b. In contrast, DAW, destabilized by parallel passing electrons, is insensitive to the pedestal T_i profile. The critical transition toroidal mode number n_{crit} between PBM and DAW increases with the pedestal scale factor F_i increases. PBM linear growth rate dominates over DAW in the whole n = 5-60 range for $F_i \geq 1.2$, and DAW dominates the whole n = 5–60 range for $F_i \leq 0.6$ in Fig. 5b. In Fig. 5d, we found that DAW becomes unstable with a steepened pedestal T_e profile, and PBM linear growth also increases slightly due to the change of ballooning drive with total pressure. In this sense, the magnitude of PBM tracks F_i, while DAW increases with F_e. The divertor heat flux width λ_q is broadened remarkably with an increase of F_i (Fig. 5e) while shows much less sensitivity to the electron temperature and the upper pedestal localized DAW suggesting that DAW does not spread to the SOL, and so does not broaden λ_q directly. The results of this numerical "experiment" are summarized in Table 1.

On how the pedestal modes link to the divertor heat flux, we argue it is through the turbulence spreading. The SOL of these plasmas is linearly stable, so turbulence there is necessarily dominated by turbulence spreading from the pedestal, across the separatrix. Over the past few decades,

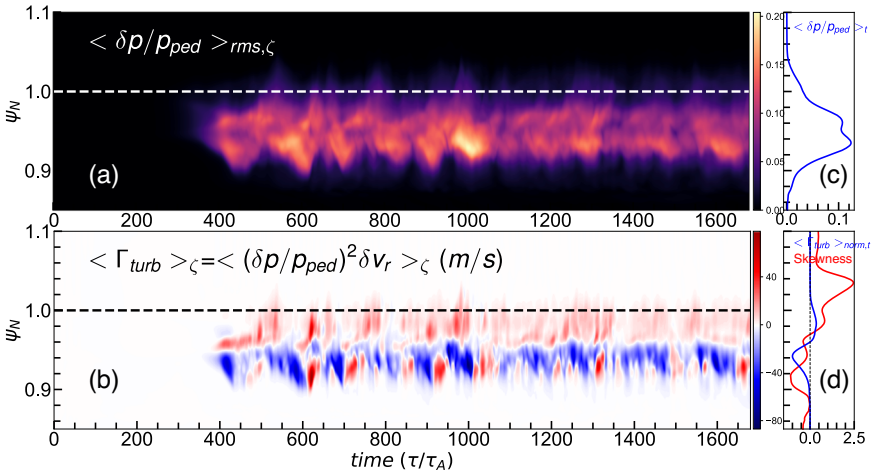

Fig. 6 | Nonlinear simulation of the DIII-D turbulent quiescent-H (QH) mode. a normalized pressure perturbation; **b** normalized turbulence intensity flux. Here $\delta p, p_{ped}$ and δv_r are the perturbed pressure, equilibrium pedestal top pressure, and perturbed radial velocity in BOUT + + modeling. The horizontal axis is the time in Alfvén time, and the vertical axis is the normalized poloidal magnetic flux. The horizontal dashed line indicates the location of the separatrix. **c** The time-averaged pressure perturbation (blue) in the saturation phase. **d** The time-averaged turbulence intensity flux (blue) in the saturation phase, and normalized by its radial maximum absolute value; radial skewness of the pressure perturbation (red).

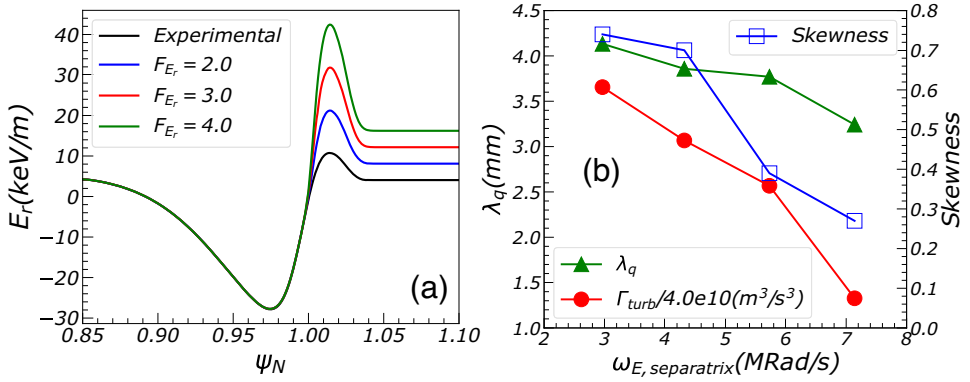

Fig. 7 | The impact of separatrix *E*×*B* shearing rate on the divertor heat flux width. a Scan of scrape-off-layer SOL E_r profile; **b** Divertor heat flux width λ_q (green), turbulence intensity flux Γ_{turb} (red) and skewness $\mathscr{S}$ of pressure perturbation (blue) at the outboard-mid-plane separatrix as a function of separatrix $E \times B$ shearing rate.

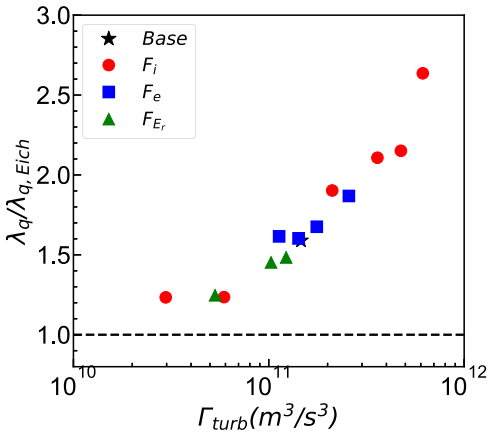

Fig. 8 | The divertor heat flux width broadens with the turbulence intensity increases. Normalized divertor heat flux width as a function of flux surface and time-averaged turbulence intensity flux Γ_{turb} across the separatrix. Different symbols demonstrate the different scans on the profiles.

significant progress has been made in understanding turbulence spreading[27] by theory, simulations[28–31] and experiments[32–36]. The flux of turbulence intensity is calculated to quantify the spreading into the SOL in the turbulent QH plasma studies here. Figure 6a, b shows turbulence spreading of normalized pressure perturbation and normalized turbulence intensity flux. Turbulence is generated inside of the pedestal, at $\psi_N = 0.96$ (as shown in Fig. 6a). The negative and positive turbulence intensity fluxes in Fig. 6b indicate the inward and outward spreading of turbulence intensity. The turbulence spreads from the pedestal peak gradient to the separatrix and enters the SOL, from the linearly most unstable zone to the linearly stable zone. The time-averaged pressure perturbation and turbulence intensity flux are shown in Fig. 6c, d. The skewness of pressure perturbation is also plotted in Fig. 6d. The skewness of pressure perturbation is studied to clarify the physics of turbulence spreading, which is associated with the birth and propagation of blob (filament) and void structures[37–41]. Positive skewness indicates the higher-than-average pressure 'blobs' and negative skewness indicates 'holes'. One sees that the zero-crossing point of skewness and turbulence intensity flux are well-correlated, and situated at the location of maximal turbulence generation, $\psi_N = 0.96$–0.97. Both negative signs of skewness and turbulence intensity inside of $\psi_N = 0.96$ indicate inward turbulence spreading, and vice versa. The large positive skewness ($\mathscr{S} > 2$) in the SOL shows a strong, positively skewed pressure perturbation and indicates the outward spreading feature of the turbulence. Further study of the impact of turbulence spreading on divertor heat flux width will be discussed in the following sections.

The effect of turbulence spreading on the divertor heat flux width is also studied numerically with SOL E_r scans where a stronger $E \times B$ shearing rate at the separatrix is found to obstruct pedestal turbulence spreading[40] and thus narrow the divertor heat flux width. In Fig. 7a, the SOL E_r profiles are modified accordingly, so as to change the $E \times B$ shearing rate at the separatrix, thus simulating situations with different sheath potentials. To maintain the pedestal turbulence unchanged, E_r profiles inside the separatrix are kept fixed. Separatrix $E \times B$ shearing rate is defined as the form of Hahm–Burrell $E \times B$ shearing rate[42], $\omega_E = -\frac{(RB_p)^2}{B}\frac{\partial}{\partial\psi}\left(\frac{E_r}{RB_p}\right)$, where R, B_p, B, ψ and E_r are major radius, poloidal magnetic field, total magnetic field, poloidal magnetic flux and radial electric field, respectively. The separatrix $E \times B$ shearing rate ranges over ~3–7 MRad/s for these scans. As

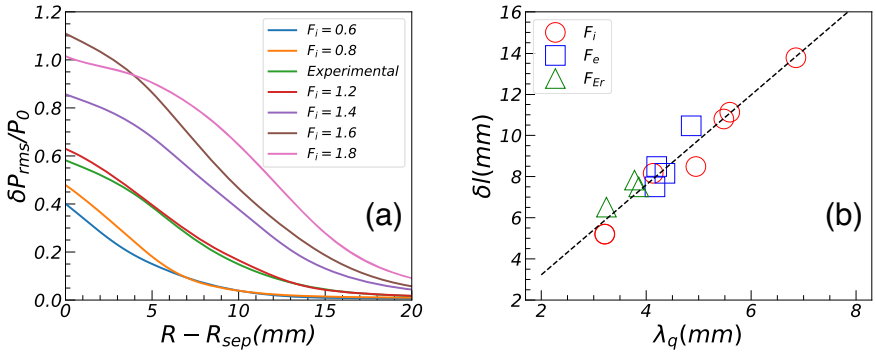

Fig. 9 | The upstream turbulence scale length is proportional to the downstream heat flux width. **a** Normalized root-mean-square pressure perturbation as a function of distance from separatrix at outboard-mid-plane in the SOL; **b** Radial scale length of pressure perturbation δl by e-folding as a function of divertor heat flux width λ_q.

the separatrix $E \times B$ shearing rate increases, the pressure perturbation skewness $\mathscr{S}$ decreases from ~0.7 to ~0.3, which is consistent with the expectation that less turbulence spreads into the SOL. The downstream divertor heat flux width λ_q also narrows accordingly, as shown in Fig. 7b. The turbulence intensity flux is also calculated for different separatrix $E \times B$ shearing rates in Fig. 7b. The turbulence intensity flux decreases with the increase of the separatrix $E \times B$ shearing rate, and it also follows the trend, as the red circles shown in Fig. 7b. All these findings indicate less turbulence spreading into the SOL when the separatrix $E \times B$ shearing rate increases, thus resulting in a narrower heat flux width.

Theoretical model

Different sets of scans discussed above of changing pedestal PBM/DAW turbulence are summarized in Fig. 8. The horizontal axis in Fig. 8 is the turbulence intensity flux across the separatrix[8,43],

$$\Gamma_{turb} = c_s^2 \left\langle \left(\frac{\delta P}{P_{sep}} \right)^2 \delta v_r \right\rangle_{\theta,\zeta,t}$$

c_s is the ion sound speed, δP, P_{sep} and δv_r are the perturbed pressure, equilibrium separatrix pressure and perturbed radial velocity form BOUT++ nonlinear simulation, bracket represents the flux-surface and time average in the nonlinear saturation phase, respectively. The vertical axis is the ratio of BOUT++ simulated heat flux width to the Eich scaling value. We find that the divertor heat flux width is close to the Eich scaling when the turbulence intensity flux is weak. λ_q exceeds the Eich scaling prediction when the turbulence intensity flux exceeds a threshold, $\Gamma_{\varepsilon,crit} \sim 1.0\text{e}11\text{m}^3/\text{s}^3$. A similar trend of λ_q is observed for different sets of PBM/DAW mode shearing rate scans. The threshold behavior is similar to Fig. 6 in ref. 8 and Fig. 2 in ref. 6 which show that the magnetic drift dominates the cross-field SOL heat transport when turbulence intensity is sufficiently weak. When the turbulence intensity flux is sufficiently large, turbulence will overtake the neoclassical cross-field transport and the divertor heat flux width increases monotonically with increasing turbulence intensity flux Γ_{turb}. Figure 8 demonstrates the connection between the pedestal turbulence characteristics and the downstream heat flux width.

The proportionality between the heat flux width and SOL mode scale length is demonstrated in Fig. 9. Normalized pressure perturbations with different T_i pedestals are shown in Fig. 9a. The normalized pressure perturbation increases in the midplane pedestal and SOL region, and turbulence spreads deeper into the far SOL region with a steepened T_i pedestal. A more extended 'tail' of the turbulence intensity profile in the SOL is observed when stronger PBM turbulence is excited in the pedestal, as shown in Fig. 9a. In Fig. 9b), the radial scale lengths of pressure perturbations at the outboard-mid-plane are quantified by e-folding estimation. The turbulence intensity scale length sets the effective mixing length in the SOL. A linear relation between the upstream turbulence intensity scale length δl for the SOL and downstream divertor heat flux width λ_q is demonstrated for different sets of scans, including pedestal T_i, T_e and SOL E_r. These findings reinforce the importance of the turbulence-broadening effect on the divertor heat flux width.

Conclusions

In conclusion, this study investigates how the pedestal turbulence can broaden the divertor heat flux width. We focused on DIII-D QH mode plasmas in the absence of ELMs where heat flux widths that are broad relative to Eich scaling are experimentally observed. Heat flux widths in broadband QH-mode are measured to increase with stronger turbulence at the separatrix. The turbulence consists of an ion-directed peeling-ballooning mode extending radially to the SOL, and an electron-directed drift Alfvén wave localized at the upper pedestal. The pedestal ion/electron temperature profiles are varied to study the role of different scale modes in broadening the divertor heat flux width λ_q. We showed that the ion-directed peeling-ballooning mode, spreads turbulence intensity into the SOL and thus efficiently broadens the λ_q. The heat flux width λ_q drops for stronger separatrix $E \times B$ shearing rate, leading to less a positively skewed perturbation and reduced spreading into the open field line region.

All these results are consistent with the theory of turbulence spreading and the calculation of turbulence intensity flux Γ_{turb} across the separatrix, which shows a broader heat flux width when the turbulence intensity flux exceeds a threshold. In particular, this crucial result establishes the connection between pedestal turbulence and downstream heat flux width. The divertor heat flux width is also found to show a positive correlation to the skewness of pressure perturbations and be proportional to the scale length of turbulence in the SOL at the outboard midplane. Note that, this paper focuses on the ion-directed peeling-ballooning turbulence and the electron-directed drift-Alfvénic turbulence with a reduced two-fluid model; further types of turbulences by including kinetic effects, i.e. trapped electron mode (TEM) turbulence[5,15] and micro-tearing mode (MTM) turbulence could also broaden the heat flux width by the spreading and entrainment process in the SOL. More generally, this work, numerically-theoretically-experimentally, supports the merit of turbulent pedestals. These could have a broader heat flux width that exceeds that predicted by the Heuristic drift scaling law, while simultaneously maintaining good core confinement. However, it is worth noting that a downside of pedestal MHD/drift wave turbulence would lead to some degradation of pedestal performance. Note that current modeling doesn't have a self-consistent flux originated from the core and the full physics of core-edge coupling. It is crucial, then to examine trade-offs, through dedicated experiments and flux-driven modeling, so as to find an optimum solution for future reactors, like ITER and beyond.

Methods

DIII-D tokamak

The DIII-D tokamak is the largest magnetic fusion experiment in the United States, supported by the U.S. Department of Energy Office of Science. The tokamak consists of a toroidal vacuum chamber surrounded by coils that produce the magnetic field to confine and shape the plasma. It has a major radius of 1.67 m and a minor radius of 0.67 m, with a toroidal magnetic field of up to 2.2 T. The plasma is created by applying a voltage to ionize a small

amount of gas injected into the vacuum chamber and drive a large, toroidal electrical current. The plasma is then quickly heated to a high temperature by injection of high-power neutral beams (< 16 MW), while additional gas fueling increases the density. More information can be found in ref. 44.

BES measurements for pedestal turbulence

The beam emission spectroscopy (BES)[45] diagnostic is applied for the study of dynamics of long-wavelength ($k_\perp < 3cm^{-1}$) density turbulence structures on DIII-D. A 64-channel BES system is configured with an 8 × 8 grid of discrete channels that image an approximately 7 × 9 cm region at the outboard midplane with the sampling frequency of 1 MHz, thus providing a modest spatial resolution, high throughput, high-time resolution turbulence imaging system.

Langmuir probe measurements for divertor heat flux width

The probe[46] tips are dome-type shape with 6 mm diameter, 1 mm height above tile surface, and ~1.5 cm separation at the outer divertor target plate. They are operated in a single-probe mode with a 1 kHz sweeping frequency. A multi-point median filter was applied to the data from each probe and the error bars were given by calculating the median absolute deviation.

IRTV infrared imaging measurements for divertor heat flux width

Heat flux measurements are performed via infrared thermography[47]. The IRTV diagnostic is used to measure the surface temperature of the lower divertor tiles in the proximity of the outer strike point. The THEODOR code is used to solve the heat conduction equation and derive the perpendicular heat flux. Parallel heat flux is derived from the perpendicular heat flux taking into account of the field line incident angle. IRTV measurements are acquired at 12 kHz with a spatial resolution of 2 mm per pixel. Note that the spreading factor sets an upper limit, S = 1.5 mm, to get reasonable fitting results.

Numerical modeling

The BOUT + + code[19,21,24] is six-field module us used for numerical modeling, which is based on Braginskii equations and evolves the ion density, ion/electron temperature, ion parallel velocity, vorticity, and magnetic vector potential. The simulation domain covers the pedestal and SOL region in normalized poloidal flux ψ_N = 0.85–1.10, with a grid resolution of radial $n_\psi = 256$, field-aligned $n_y = 64$ and binormal $n_z = 64$ in the field-aligned coordinate on simulating a 1/5 of the torus. The simulation contains $n = 5$, 10, 15, …, 80 toroidal number modes. PVODE, an implicit time integration method, is used for time-stepping and the simulation continuous until the divertor heat flux is well saturated. Realistic Spitzer-Härm resistivity is used in the modeling. Sheath boundary conditions are applied on the divertor targets. In the radial direction, the main ion and carbon density and temperatures are are set to be Neumann, e.g. $\partial n/\partial\psi = 0$ to let them freely evolve. Neumann boundary conditions are also applied to the vorticity and parallel velocity and Zero-Laplacian boundary condition, $\Delta A_\parallel = 0$, is applied to the parallel vector potential. The pedestal plasma profiles are based on the well-converged reconstructed equilibrium using EFIT code[48]. The parallel thermal conductivity in the flux limited form is given by, $\kappa_{eff,j} = \frac{\kappa^{SH}_{\parallel,j}\kappa^{FS}_{\parallel,j}}{\kappa^{SH}_{\parallel,j}+\kappa^{FS}_{\parallel,j}}$, where j signifies ion or electron, $\kappa^{SH}_{\parallel,i} = 3.9 n_i v^2_{th,i}/\nu_i$ and $\kappa^{SH}_{\parallel,e} = 3.2 n_e v^2_{th,e}/\nu_e$ are the Spitzer-Härm parallel thermal conductivities, $v_{th,j}$ and ν_j are the thermal velocity and collision rate for the j species. $\kappa^{FS}_{\parallel,j} = \alpha_j n_j v_{th,j} q R_0$ is the free streaming parallel thermal conductivity, where q is the safety factor and R_0 is the major radius. A realistic E_r profile from the pedestal up to SOL calculated from the ion momentum balance equation based on Charge Exchange Recombination (CER) Spectroscopy System[49,50] in DIII-D is used in the simulation. The diamagnetic E_r arising from the zonal pressure component is retained, while the Reynolds Stress-induced zonal flow is omitted in the simulation, which is in line with the approach in ref. 51 and other publications. Carbon is the major impurity considered in the modeling: the equilibrium carbon density and temperature profiles are from the DIII-D CER system; carbon and main ion temperature are set to be the same. Divertor heat flux widths are measured in the fully saturated stage of the simulation. More details about the model can be found in Supplementary note 1 and on saturation in Supplementary note 2.

Data availability

Raw data were generated at the DIII-D facility. Derived data that support the plots within this paper and other findings of this study are available from the corresponding author upon reasonable request.

Code availability

The computer code used to generate results that are reported in the paper is available from the authors on reasonable request.

Received: 17 October 2023; Accepted: 5 March 2024;
Published online: 15 March 2024

References

1. Banacloche, S. et al. Socioeconomic and environmental impacts of bringing the sun to earth: a sustainability analysis of a fusion power plant deployment. *Energy* **209**, 118460 (2020).
2. Linke, J. High heat flux performance of plasma facing materials and components under service conditions in future fusion reactors. *Fusion Sci. Technol.* **49**, 455 (2006).
3. Eich, T. et al. Inter-ELM power decay length for JET and ASDEX upgrade: measurement and comparison with heuristic drift-based model. *Phys. Rev. Lett.* **107**, 215001 (2011).
4. Goldston, R. J. Heuristic drift-based model of the power scrape-off width in low-gas-puff H-mode tokamaks. *Nucl. Fusion* **52**, 013009 (2012).
5. Chang, C. S. et al. Gyrokinetic projection of the divertor heat-flux width from present tokamaks to ITER. *Nucl. Fusion* **57**, 116023 (2017).
6. Li, Zeyu et al. Prediction of divertor heat flux width for ITER using BOUT++ transport and turbulence module. *Nucl. Fusion* **59**, 046014 (2019).
7. Xu, X. Q. et al. Simulations of tokamak boundary plasma turbulence transport in setting the divertor heat flux width. *Nucl. Fusion* **59**, 126039 (2019).
8. Chu, X. et al. SOL width broadening by spreading of pedestal turbulence. *Nucl. Fusion* **62**, 066021 (2022).
9. Kobayashi, M. et al. Turbulence spreading into an edge stochastic magnetic layer induced by magnetic fluctuation and its impact on divertor heat load. *Phys. Rev. Lett.* **128**, 125001 (2022).
10. Burrell, K. H. et al. Quiescent H-mode plasmas in the DIII-D tokamak. *Plasma Phys. Control. Fusion* **44**, A253 (2002).
11. Burrell, K. H. et al. Quiescent H-mode plasmas with strong edge rotation in the cocurrent direction. *Phys. Rev. Lett.* **102**, 155003 (2009).
12. Burrell, K. H. et al. Discovery of stationary operation of quiescent H-mode plasmas with net-zero neutral beam injection torque and high energy confinement on DIII-D. *Phys. Plasmas* **23**, 056103 (2016).
13. Chen, X. et al. Stationary QH-mode plasmas with high and wide pedestal at low rotation on DIII-D. *Nucl. Fusion* **57**, 022007 (2017).
14. Houshmandyar, S. et al. Explaining the lack of power degradation of energy confinement in wide pedestal quiescent H-modes via transport modeling. *Nucl. Fusion* **62**, 056024 (2022).
15. Ernst, D. R. et al. Broadening of the Divertor Heat Flux Profile in High Confinement Tokamak Fusion Plasmas with Edge Pedestals Limited by Turbulence in DIII-D, http://arxiv.org/abs/2403.00185 (2024).
16. Chen, X. et al. Bifurcation of quiescent H-mode to a wide pedestal regime in DIII-D and advances in the understanding of edge harmonic oscillations. *Nucl. Fusion* **57**, 086008 (2017).
17. Chen, X. et al. Expanding the parameter space of the wide-pedestal QH-mode towards ITER conditions. *Nucl. Fusion* **60**, 092006 (2020).

18. Burrell, K. H. et al. Reactor-relevant quiescent H-mode operation using torque from non-axisymmetric, non-resonant magnetic fields. *Phys. Plasmas* **19**, 056117 (2012).
19. Zeyu, L. et al. Numerical modeling of pedestal stability and broadband turbulence of wide-pedestal QH-mode plasmas on DIII-D. *Nucl. Fusion* **62**, 076033 (2022).
20. McKee, G. et al. The beam emission spectroscopy diagnostic on the DIII-D tokamak. *Rev. Sci. Instrum.* **70**, 913 (1999).
21. Dudson, B. D. et al. BOUT++: A framework for parallel plasma fluid simulations. *Comput. Phys. Commun.* **180**, 1467–1480 (2009).
22. Xia, T. Y. et al. Nonlinear fluid simulation of particle and heat fluxes during burst of ELMs on DIII-D with BOUT++ code. *Nucl. Fusion* **55**, 113030 (2015).
23. Chen, B. et al. Edge turbulence and divertor heat flux width simulations of Alcator C-Mod discharges using an electromagnetic two-fluid model. *Nucl. Fusion* **57**, 116025 (2017).
24. Xia, T. Y. et al. Divertor heat flux simulations in ELMy H-mode discharges of EAST. *Nucl. Fusion* **57**, 116016 (2017).
25. Li, Nami et al. Characteristics of grassy ELMs and their impact on the divertor heat flux width. *Nucl. Fusion* **62**, 096030 (2022).
26. Li, Zeyu et al. Edge localized mode characteristics and divertor heat flux during stationary and transient phase for CFETR hybrid scenario. *Plasma Phys. Control. Fusion* **63**, 035006 (2021).
27. Hahm, T. S. & Diamond, P. H. Mesoscopic transport events and the breakdown of Fick's law for turbulent fluxes. *J. Korean Phys. Soc.* **73**, 747–792 (2018).
28. Hahm, T. S. et al. Turbulence spreading into the linearly stable zone and transport scaling. *Plasma Phys. Control. Fusion* **46**, A323 (2004).
29. Gurcan, O. D. et al. Radial transport of fluctuation energy in a two-field model of drift-wave turbulence. *Phys. Plasmas* **13**, 052306 (2006).
30. Lin, Z. et al. Turbulence spreading and transport scaling in global gyrokinetic particle simulations. *Phys. Plasmas* **11**, 1099 (2004).
31. Garbet, X. et al. Radial propagation of turbulence in tokamaks. *Nucl. Fusion* **34**, 963 (1994).
32. Estrada, T. et al. Signatures of turbulence spreading during the H–L back-transition in TJ-II plasmas. *Nucl. Fusion* **51**, 032001 (2011).
33. Grenfell, G. et al. The impact of edge radial electric fields on edge–scrape-off layer coupling in the TJ-II stellarator. *Nucl. Fusion* **60**, 014001 (2020).
34. Ting, W. et al. Effect of edge turbulent transport on scrape-off layer width on HL-2A tokamak. *Plasma Sci. Technol.* **23**, 02510 (2021).
35. Long, T. et al. Enhanced particle transport events approaching the density limit of the J-TEXT tokamak. *Nucl. Fusion* **61**, 126066 (2021).
36. Wu, T. et al. How turbulent transport broadens the heat flux width: local SOL production or edge turbulence spreading? *Nucl. Fusion* **63**, 126001 (2023).
37. Wang, W. X. et al. Nonlocal properties of gyrokinetic turbulence and the role of E×B flow shear. *Phys. Plasmas* **14**, 072306 (2007).
38. D'Ippolito, D. A. et al. Convective transport by intermittent blob-filaments: comparison of theory and experiment. *Phys. Plasmas* **18**, 060501 (2011).
39. Krasheninnikov, S. On scrape off layer plasma transport. *Phys. Lett. A* **283**, 368 (2001).
40. Boedo, J. A. et al. Scaling of plasma turbulence suppression with velocity shear. *Nucl. Fusion* **42**, 117–121 (2002).
41. Manz, P. et al. Origin and turbulence spreading of plasma blobs. *Phys. Plasmas* **22**, 022308 (2015).
42. Burrell, K. H. et al. Effects of ExB velocity shear and magnetic shear on turbulence and transport in magnetic confinement devices. *Phys. Plasmas* **4**, 1499–1518 (1997).
43. Nami, L. et al. How fluctuation intensity flux drives SOL expansion. *Nucl. Fusion* **63**, 124005 (2023).
44. Luxon, J. L. A Brief Introduction to the DIII-D Tokamak. *Fusion Sci. Technol.* **48**, 828 (2005).
45. McKee, G. R. et al. Wide-field turbulence imaging with beam emission spectroscopy. *Rev. Sci. Instrum.* **81**, 10D741 (2010).
46. Watkins, J. G. et al. High heat flux Langmuir probe array for the DIII-D divertor plates. *Rev. Sci. Instrum.* **79**, 10F125 (2008).
47. Lasnier, C. J. et al. Survey of target plate heat flux in diverted DIII-D tokamak discharges. *Nucl. Fusion* **38**, 1225 (1998).
48. Lao, L. L. et al. Reconstruction of current profile parameters and plasma shapes in tokamaks. *Nucl. Fusion* **25**, 1611 (1985).
49. Chrystal, C. et al. Improved edge charge exchange recombination spectroscopy in DIII-D. *Rev. Sci. Instrum.* **87**, 11E512 (2016).
50. Burrell, K. H. et al. Improved charge coupled device detectors for the edge charge exchange spectroscopy system on the DIII-D tokamak. *Rev. Sci. Instrum.* **72**, 1028 (2021).
51. Xu, X. Q. et al. Nonlinear simulations of peeling-ballooning modes with anomalous electron viscosity and their role in edge localized mode crashes. *Phys. Rev. Lett.* **105**, 175005 (2010).
52. Eich, T. et al. Scaling of the tokamak near the scrape-off layer H-mode power width and implications for ITER. *Nucl. Fusion* **53**, 093031 (2013).

Acknowledgements

Z.L. would like to thank Dr. R.J. Groebner and Dr. C.C. Petty in General Atomics, and Dr. M.W. Shafer in Oak Ridge National Laboratory for revising and commenting on the manuscript. Additionally, Z.L. would also like to extend thanks to Dr. D.R. Ernst for the discussions that helped refine the manuscript. This material is based upon work supported by the U.S. Department of Energy, Office of Science, Office of Fusion Energy Sciences, using the DIII-D National Fusion Facility, a DOE Office of Science user facility, under Awards: DE-FC02-04ER54698, LLNL-JRNL-829769, DE-AC52-07NA27344, DE-FG02-08ER54999, DE-SC0019352 and LLNL-led SciDAC ABOUND Project SCW1832. This research used resources of the National Energy Research Scientific Computing Center, a DOE Office of Science User Facility supported by the Office of Science of the U.S. Department of Energy under Contract No. DE-AC02-05CH11231 using NERSC award FES-ERCAP0020598.

Author contributions

Z.L. led the experimental data analysis, numerical simulations, and manuscript writing. X.C. led the experimental demonstration and conceived the original idea. P.D. conceived the critical physics picture and guided the data analysis and manuscript writing. X.Q.X. supported BOUT + + code and guided the simulation. X.Q., Z.Y. and F.K. provided data analysis for BES for pedestal and SOL turbulence. H.Q.W. provided data analysis for Langmuir Probes for divertor heat flux widths. F.S. and R.H. provided data analysis for the IR camera for divertor heat flux widths. G.Y., G.M. and Z.Y. offered general comments on the research.

Competing interests

The authors declare no competing interests.

Additional information

Supplementary information The online version contains supplementary material available at https://doi.org/10.1038/s42005-024-01590-0.

Correspondence and requests for materials should be addressed to Zeyu Li.

Peer review information *Communications Physics* thanks Patrick Tamain for their contribution to the peer review of this work. A peer review file is available.